Main Manuscript for

Disrupted Development of the mPFC-Thalamic Circuit in the Mouse Shank3$^{-/-}$ model of Autism

Gabrielle Devienne, Gil Vantomme, John R Huguenard*

Department of Neurology and Neurological Sciences, Stanford University, Stanford, CA, USA.

Corresponding author: John R Huguenard, Stanford Neuroscience Building S189, 290 Jane Stanford Way, Stanford, CA 94305-5088

Email: huguenard@stanford.edu

Author Contributions: Gabrielle Devienne: Data collection, Conceptualization, Software, Formal analysis, Investigation, Writing - Original Draft, Visualization, Funding acquisition; Gil Vantomme: Data collection, Software, Validation, Formal analysis, Investigation; John R Huguenard: Conceptualization, Software, Writing - Original Draft, Funding acquisition.

Competing Interest Statement: Authors have no conflict of interest to declare.

Keywords: prefrontal cortex, autism, electrophysiology.

This PDF file includes:

Main Text
Figures 1 to 6

Abstract: Autism Spectrum Disorders (ASDs) are a group of neurodevelopmental disorders with heterogeneous causes, and are characterized by communication deficits, impaired social interactions, and repetitive behaviors. Despite numerous studies in mouse models focused on pathophysiological circuit mechanisms of ASD in mature animals, little is known regarding ASD onset and its evolution through development. The medial prefrontal cortex (mPFC) is crucial for higher-order cognitive functions and social behavior, thus key to understanding ASD pathology. To explore early developmental disruptions in the mPFC, we used the *Shank3* knockout (Shank3$^{-/-}$) mouse model. SHANK3 is crucial for glutamatergic synapse maturation, and the Shank3$^{-/-}$ mouse has been well-characterized for displaying ASD-related behavioral phenotypes. We investigated network, cellular, and synaptic changes within the mPFC and in its projections to the mediodorsal thalamus (MD) at two developmental stages, preweaning (P14) and adulthood (>P55). Our findings reveal early synaptic deficits at P14 both within the mPFC and in its projections to the MD accompanied by alterations in mPFC network activity and reduced excitability of excitatory neurons, overall suggesting hypofunction. Interestingly, behavioral deficits were already detectable by P11, preceding the observation of synaptic changes at P14. By adulthood, these early synaptic and cellular alterations progressed to global dysfunction, characterized by mPFC network hyperfunction and layer 5 pyramidal cell hyperexcitability, accompanied by augmented glutamatergic signaling to MD with enhanced action potential production. These results suggest that early synaptic changes may precede and interact with behavioral deficits, potentially leading to compensatory mechanisms that contribute to more pronounced mPFC dysfunction later in development. This study highlights the complex dynamic progression of mPFC deficits in ASD and emphasizes the potential impact of targeting early synaptic alterations to mitigate later behavioral and cognitive deficits.

48 **Introduction:**

49 Autism Spectrum Disorders (ASDs) refer to a group of neurodevelopmental disorders characterized
50 by communication deficits, impaired social interaction, and repetitive behaviors. ASD arises from complex
51 etiologies including genetic causes and prenatal insults, making it difficult to precisely determine its onset
52 across individuals. In humans, the behavioral deficits related to ASD are generally first observed around the
53 second year of life(1,2), a period associated with rapid maturation of the medial prefrontal cortex (mPFC)(3).
54 Abnormal mPFC development is hypothesized to contribute to ASD symptoms(4–6), given its critical role in
55 regulating social behavior(5,7–9). In mouse, communication deficits can be perceived in the early postnatal
56 periods (pre-weaning; <P21)(10,11) a critical window for morphological and functional mPFC development
57 (12). It is around the same period that mPFC develops long range connections with subcortical areas(12,13)
58 including reciprocal connections with the mediodorsal thalamus (MD)(14).

59 SHANK3, a scaffolding protein critical for glutamatergic synapse maturation(15), is a leading genetic
60 cause of ASD(16,17). The Shank3$^{-/-}$ mouse model(11) recapitulates many ASD-related phenotypes,
61 including social deficits and communication impairments. Interestingly, SHANK3 protein levels naturally
62 decline around P14 during normal development(18), coinciding with a reduction in connectivity between the
63 mPFC and the MD(19). This developmental window offers a unique opportunity to investigate how early
64 synaptic changes might predispose the mPFC-MD circuit to later dysfunction. By studying the Shank3$^{-/-}$
65 model at both P14 and adulthood (>P55), we aim to identify whether early synaptic alterations set the stage
66 for later deficits in network and behavioral function.

67 To investigate mPFC disruptions in Shank3$^{-/-}$ mice, we compared network, cellular, and synaptic
68 properties at P14 and adulthood (>P55). Behavioral assessments confirmed communication deficits as early
69 as P11(11) as well as social deficits in adulthood(11,20), emphasizing the early onset and persistence of
70 ASD-related symptoms. Electrophysiological methods, including local field potential (LFP) and whole-cell
71 patch-clamp recordings, were used to examine mPFC activity. We also tested mPFC-MD circuit function
72 using optogenetic stimulation of mPFC axons and intracellular recordings in MD cells.

73 Our findings reveal a dynamic progression of mPFC deficits in Shank3$^{-/-}$ mice. At P14, mPFC
74 hypoexcitability was observed in upper layer pyramidal cells, with synaptic excitatory-inhibitory imbalance
75 in layer 5. Despite an overall mPFC network hypoexcitability, optogenetic stimulation of mPFC-MD
76 projections revealed exuberant and long-lasting synaptic excitation in MD cells, an early sign of circuit
77 hyperexcitability. In adulthood, pronounced mPFC network hyperactivity emerged, particularly in layer 5
78 pyramidal cells that project to the MD. Long lasting excitatory synaptic responses in MD cells were
79 persistently augmented in Shank3$^{-/-}$ mice, indicating long-term disruptions in mPFC-MD connectivity.

80 These results show that early synaptic changes in Shank3$^{-/-}$ mice precede pronounced network
81 dysfunction in adulthood. Mixed findings at P14 suggest compensatory mechanisms may temporarily mask

82 mPFC dysfunction, highlighting critical periods of vulnerability in ASD and the potential for early interventions
83 to mitigate long-term deficits.

84 **Results:**

85 **Early emergence of social behavioral deficits in Shank3$^{-/-}$ mice.**

86 To assess the development of potential SHANK3-related behavioral deficits, we tested WT and Shank3$^{-/-}$
87 mice at two distinct developmental stages: pups (P11) and adults (>P55). Given the limited mobility of pre-
88 weaning pups, ultrasonic vocalizations (USV) have be used as a proxy of social behavior(21). Upon social
89 isolation Shank3$^{-/-}$ P11 pups produced many fewer calls compared to their wild type (WT) littermates (Figure
90 1 A-D; mean ± sem; WT: 253 ± 58 calls; Shank3$^{-/-}$: 61 ± 30 calls; testing period 8 minutes; Mann-Whitney,
91 p=0.01). Consistent with social deficits persisting into adulthood, mature Shank3$^{-/-}$ mice failed to show a
92 social preference in a social interaction test, showing similar times with either a novel inanimate object or a
93 novel conspecific mouse. In contrast, adult WT mice showed a strong social preference (Figure 1 E-G;
94 interaction time, mean ± sem; WT: mouse, 33.1 ± 4.95, object, 15.8 ± 1.95 %, paired t-test, p= 0.02; Shank3^{-}
95 $^{/-}$: mouse, 14.6 ± 5.62, object: 15.8 ± 5.91%, paired t-test, p= 0.89). These results align with previous
96 literature on ASD mouse models(22–24), including the complete Shank3 knockout used here(11). We
97 therefore confirm that behavioral deficits in this model begin as early as P11, which correlates with a period
98 of critical development of the corticothalamic network connecting the medial prefrontal cortex (mPFC) to the
99 mediodorsal thalamus (MD) (12,14), an important circuit related to social behavior(25).

100 **Developmental progression of hyperexcitability in the mPFC network**

101 To investigate potential SHANK3-related disruptions in mPFC development, we first employed an *in vitro*
102 extracellular recording approach to evaluate network excitability. We obtained coronal brain slices
103 containing the mPFC from Shank3$^{-/-}$ mice and WT littermates at different developmental stages, including
104 P11, P14, and adulthood (Figure 2 and Figure S1). Using a 16-shank linear silicon probe array positioned
105 normal to the pial surface of mPFC, we recorded network activity in the form of local-field potentials (LFPs).
106 Local electrical stimulation of deep layers evoked multicomponent LFPs that could be observed across all
107 cortical layers, demonstrating engagement of intra-cortical circuits (Figure 2A). To localize the LFP signals
108 to different cortical layers, we calculated the current source density(26) (CSD) as the second spatial
109 derivative of the LFP (Figure 2B and C). This allowed us to compare mPFC network differences between
110 Shank3$^{-/-}$ mice and WT littermates. We observed matched pairs of sinks and sources in the CSD profiles
111 following local electrical stimulation in the deep layers. Sinks are negative CSD signals generally attributed
112 to the movement of cations from the extracellular space into the cells during synaptic excitation. Given
113 conservation of charge, such ionic current flow must be matched with a paired outward flow of cations
114 (sources) from these cells at a distance from the original sinks. Synaptic inhibition has the opposite
115 sinks/source polarity as it is mainly associated with anionic, rather than cationic, current flow. Accordingly,
116 sources/sinks cannot unambiguously be associated with either excitation or inhibition. However given that

117 the majority of synapses in neocortical circuits are excitatory(27–29), sinks will generally be dominated by
118 excitatory synaptic signals, and sources with their return path. We applied a subtractive pharmacological
119 approach to isolate components of the CSD signal, to reveal distinct pre- and post-synaptic components,
120 with the post-synaptic components essentially blocked by DNQX and CPPene, AMPA and NMDA receptor
121 antagonists (Figure S1A2, B), and presynaptic components blocked by TTX.

122 We initially assessed mPFC excitability at the two stages that we had previously characterized behaviorally,
123 P11 and adult. At P11 we observed LFP and CSD components generally comparable to what was observed
124 in adult mice, although with somewhat simpler features especially noted as more monophasic responses,
125 consistent with the immature state of the network at P11 (Figure 2A, vs. Figure S1C). We did not detect any
126 differences between Shank3$^{-/-}$ mice and their WT littermates at this stage. We then selected P14 as the
127 next developmental time point. This is a developmental stage marked by significant changes in SHANK3
128 protein levels(18). The CSD signal at P14 showed sinks and sources across layers that were more complex
129 (multiphasic) than at P11, and more similar to the CSD responses in adults. At P14, both the previously
130 identified postsynaptic sinks and sources (Figure S1B) were similar between Shank3$^{-/-}$ mice and WT
131 littermates. However, we observed a significant reduction of the presynaptic source located in layer 5 (Figure
132 2C, component 3),with little to no reduction in presynaptic sink in layer 2/3 (component 1) in Shank3$^{-/-}$ mice
133 compared to WT littermates (Figure 2CD P14; two-way ANOVA with repeated measures: genotype $p=0.03$,
134 stimulation $p<0.0001$, interaction $p<0.0001$ for the layer 5 presynaptic source). This reduction in CSD signal
135 may reflect a hypofunction of mPFC at this stage of development, in particular of the presynaptic recruitment
136 of the cortical network. By contrast, at adulthood, mPFC slices from Shank3$^{-/-}$ mice showed an overall
137 *increase* in sinks and sources across layers (components 1-4, Figure 2B-D). Closer inspection revealed that
138 this overall increase in CSD signal in adult is mediated by an increase in the peak amplitude of the layer 2/3
139 presynaptic sink and the layer 5 presynaptic source and postsynaptic sink (Figure 2CD Adults; 2-way
140 ANOVA with repeated measure, layer 2/3 presynaptic sink: genotype $p=0.004$, stimulation $p<0.0001$,
141 interaction $p<0.0001$; layer 5 presynaptic source: genotype $p=0.001$, stimulation $p<0.0001$, interaction
142 $p<0.0001$, layer 5 postsynaptic sink: genotype $p=0.01$, stimulation $p<0.0001$, interaction $p=0.04$). There is
143 also a trend for an increase in the peak amplitude of layer 2/3 postsynaptic source in adult Shank3$^{-/-}$ mice
144 (Figure 2D Adults; 2-way ANOVA with repeated measure, layer 2/3 postsynaptic source: genotype $p=0.051$,
145 stimulation $p<0.0001$, interaction $p=0.08$). Altogether, these data demonstrate the emergence of a
146 hyperfunctional mPFC network between P14 and adulthood (>P55) in the Shank3$^{-/-}$ mouse model,
147 characterized by early-stage hypoexcitability at P14 followed by hyperexcitability in adulthood, reflecting a
148 developmental shift in network dynamics.

149 **Developmental emergence of hyperexcitability of layer 5 mPFC pyramidal cells.**

150 Our *in vitro* LFP experiments revealed increased mPFC network activity in Shank3$^{-/-}$ adult mice, evidenced
151 in both pre- and postsynaptic signals. These results suggest potential alterations in the properties of local
152 mPFC cells and/or in the synaptic connections within the mPFC. Excitatory pyramidal neurons in the mPFC

153 are crucial for regulating cognitive and social behavior(30). Layer 2/3 of the mPFC receives diverse long-
154 range inputs, including notable projections from the MD thalamus(31). Conversely, layer 5 of the mPFC
155 primarily projects to the MD thalamus, although not exclusively(12,32,33) as it can target other subcortical
156 areas along with the contralateral mPFC.

157 To investigate changes in cellular excitability, we recorded mPFC layer 2/3 and layer 5 pyramidal cells at
158 P14 and in adulthood (>P55). Consistent with decreased excitability observed in the LFP (Fig 2D), early in
159 development L2/3 pyramidal cells revealed hypoexcitability, in particular with a hyperpolarized resting
160 membrane potential (Figure 3A; RMP, P14; mean ± sem; WT: -58.6 ± 1.3 vs Shank3$^{-/-}$: -62.8 ± 1.3; p=0.03,
161 Welsh t-test) which is not observed in adults. In addition, we found that these cells fired significantly fewer
162 action potentials in response to depolarizing current steps (Figure 3B; 2-way ANOVA; genotype p=0.0002,
163 current injection p<0.0001, interaction p<0.0001). In adulthood this layer 2/3 hypoexcitability was no longer
164 evident (Figure 3C).

165 Various ASD mouse models have been shown to display hyperexcitability of adult mPFC layer 5 pyramidal
166 cells(5,34,35). Consistent with this, we find that in Shank3$^{-/-}$ mice layer 5 pyramidal cells have a depolarized
167 RMP (Figure 3D; RMP; Adults; mean ± sem; WT: -67 ± 1.3 vs Shank3$^{-/-}$: -63.4 ± 1.2, p=0.048, Welsh t-test).
168 Similar results were observed at P14 (Figure 3D; RMP; P14; mean ± sem; WT: -63 ± 1.3 vs Shank3$^{-/-}$: -57.4
169 ± 1.4, p=0.005, Welsh t-test). This early sign of hyperexcitability is also reflected by a higher input resistance
170 (Figure 3D; RMP; P14; mean ± sem; WT: 304 ± 29 vs Shank3$^{-/-}$: 448 ± 33, p=0.003, Welsh t-test). At P14,
171 layer 5 pyramidal cells displayed similar action potential numbers in response to a range of depolarizing
172 current injections in Shank3$^{-/-}$ and WT littermates (Figure 3E). Interestingly, in this assay Shank3$^{-/-}$ adult
173 layer 5 pyramidal cells display higher number of action potentials (Figure 3F; 2-way ANOVA; genotype p=
174 0.0058, current injection p<0.0001, interaction p<0.0001). In addition, these cells also display an increased
175 hyperpolarization induced membrane potential sag compared to their WT littermates (Figure S2 B5, p=0.04,
176 Mann Whitney test). We did not observe any alterations in individual action potential properties at any age
177 or in any layer (Figure S2).

178 Biocytin was included in our intracellular recording solution, which allowed us to recover the cellular
179 morphology of a subset of mPFC layer 5 pyramidal cells in both WT and Shank3$^{-/-}$ at P14 and in adults. A
180 Scholl analysis at both ages revealed an increase in dendritic complexity in Shank3$^{-/-}$ cells (Figure S3B; 2-
181 way ANOVA, P14, genotype p=<0.0001, distance p=<0.0001, interaction p=<0.0001; Adults, genotype
182 p=<0.0001, distance p=<0.0001, interaction p=<0.0001). Shank3$^{-/-}$ neurons had more arborizations near
183 the soma and more branches overall compared to WT, while the average neurite length was similar (Figure
184 S3C, D, E). It has been described that layer 5 pyramidal cells can be split in at least two different subtypes:
185 subcortically projecting, thick-tufted neurons that display a marked H-current and related hyperpolarization
186 induced membrane potential sag, and callosal projecting, thin-tufted neurons that display an absence in H-
187 current(36,37). To exclude the possibility that these findings represent differences in the proportions of
188 recorded cell subtypes in Shank3$^{-/-}$ vs WT animals, we measured apical dendritic shaft width in WT and

189 Shank3$^{-/-}$, and these did not show any differences (Figure S3F) suggesting that our morphological analysis
190 was performed in comparable mPFC neuron populations, such that the differences in cell morphology we
191 describe are unlikely to be explained by differences in proportion of subtypes in WT vs. Shank3$^{-/-}$ mice.
192 Overall, WT/ Shank3$^{-/-}$ mPFC layer 5 pyramidal neuron increases in excitability and dendritic complexity
193 are already present at P14 and further develop into adulthood.

194 In summary, our whole-cell patch-clamp recordings revealed signs of hypoexcitability in mPFC layer 2/3
195 pyramidal neurons in juvenile Shank3$^{-/-}$ mice. By contrast, at this stage, we already see early signs of
196 hyperexcitability in layer 5 pyramidal cells which persist with greater functional consequences in adults.

197 **Decreased E-I ratio observed at P14 and in the adult Shank3$^{-/-}$ mice**

198 A major goal in ASD research has been to find convergent mechanisms in different genetic mouse models.
199 One of the main hypotheses, as proposed by Rubenstein and Merzenich(38), is linking genetic models of
200 autism through a common mechanism of increase in excitatory-inhibitory synaptic ratio. We used whole-cell
201 voltage-clamp recordings to examine the synaptic responses in mPFC layer 2/3 and layer 5 pyramidal cells.
202 Synaptic responses were evoked using an electrical bipolar stimulating electrode placed in upper layer 2/3.
203 Excitatory post-synaptic currents (EPSCs) were recorded at V_m of -70mV and inhibitory postsynaptic
204 currents (IPSCs) at V_m of +10mV (Figure 4A). The excitatory-inhibitory ratio in Layer 2/3 mPFC pyramidal
205 cells were not different between WT and Shank3$^{-/-}$ at either P14 or in adults (Figure S4B). By contrast,
206 Shank3$^{-/-}$ mPFC layer 5 pyramidal cells displayed a reduced E-I ratio already evident at P14 (Figure 4B-C;
207 mean ± sem; P14 WT: 0.98 ±0.21, P14 Shank3$^{-/-}$: 0.4 ± 0.1, Mann Whitney test, p=0.04) and reduction
208 continued into adulthood (Figure 4B-C; mean ± sem; WT: 1.1 ± 0.3, Shank3$^{-/-}$: 0.5 ± 0.1, Mann Whitney test,
209 p=0.03). These data, in contrast to previous observations made in other ASD models, suggest that the
210 imbalance of the E-I ratio in Shank3$^{-/-}$ mice is an actual reduction in E-I ratio and is restricted to inputs to
211 layer 5 pyramidal neurons of the mPFC. Interestingly, this imbalance is observed as early as P14, indicating
212 that these alterations in synaptic function occur during early developmental stages, potentially contributing
213 to the onset and progression of ASD in Shank3$^{-/-}$ mice.

214 **Altered mPFC- MD thalamus synaptic function in Shank3$^{-/-}$ mice.**

215 As outlined above, one of the major projections of mPFC layer 5 pyramidal cells is the MD thalamus. To
216 evaluate whether the changes we observed in mPFC were associated with and potentially causative of
217 effects on downstream targets, we injected mPFC with one of two Channelrhodopsin2 expressing viruses
218 AVVDJ for P0 injections (Figure S6) and AAV1 CaMKIIa-ChR2-eYFP for adults, followed by in vivo
219 incubation for several weeks. We then recorded synaptic responses in MD cells (Figure 5A Figure S6).
220 Shank3$^{-/-}$ MD neurons showed passive properties that were indistinguishable from controls (Figure 5A1-8),
221 suggesting that the changes in intrinsic excitability we had observed were restricted to cortical locations.
222 Using 1Hz blue light stimulation, we reliably evoked optogenetic monosynaptic excitatory synaptic currents
223 (oEPSCs) as observed with a short and fixed latency (in ms; mean ± sem; P14: WT=4.3 ± 1.1; Shank3$^{-/-}$

224 =4.9 ± 1; Welch's t-test, p=0.1; adult: WT=2.6 ± 0.1; Shank3$^{-/-}$ = 2.9 ± 0.1; Welch's t-test, p=0.1). oEPSCs
225 showed similar rise time between WT and Shank3$^{-/-}$ (in ms; mean ± sem; P14: WT= 3.4 ± 1.1; Shank3$^{-/-}$ =
226 2.7 ± 1.1; Welch's t-test, p=0.1; adult: WT= 2.2 ± 0.8; Shank3$^{-/-}$ = 2.1 ± 0.8; Mann Whitney test, p=0.7) but
227 different decay time (in ms; mean ± sem; P14: WT= 16.8 ± 7.6; Shank3$^{-/-}$ = 40.9 ± 19.9; Mann Whitney test,
228 p=0.02; adult: WT= 22 ± 11.5, Mann Whitney test, p=0.03; Shank3$^{-/-}$ = 30.2 ± 19, Mann Whitney test,
229 p=0.03) (Figure 5B). Thus, mPFC efferents generate longer lasting synaptic currents in Shank3$^{-/-}$ MD
230 neurons resulting in an overall greater synaptic charge compared to littermate WT controls. The peak
231 evoked synaptic current amplitudes did not differ between WT and Shank3$^{-/-}$ mice (Figure S5B1-2),
232 suggesting that the observed differences in EPSC decay rate were unlikely to be due to any differences in
233 viral efficiency or spread from injection site.

234 We noticed that during 10 Hz trains, the synaptic current did not fully decay to baseline between individual
235 responses of the train (Figure 5C). We refer to this build-up as the persistent part of the synaptic response,
236 which accumulates over the course of the oEPSC train. We classified MD neurons regarding whether they
237 showed a persistent response based on the amplitude of the persistent current at the end of the oEPSC
238 train (just before oEPSC #10, Figure 5C1) greater than 10 pA. In Shank3$^{-/-}$ mice both the incidence and
239 amplitude and of the persistent synaptic current showed a developmental progression. At P14 only 3/11
240 WT cells exhibited a persistent current, compared to 10/12 Shank3$^{-/-}$ cells (Figure 5C2, top, chi-square test,
241 p=0.007). In adult mice, persistent synaptic responses became more common even in WT mice, appearing
242 in about 2/3 of MD cells (22/34 cells), whereas almost all Shank3$^{-/-}$ MD cells exhibited a persistent current
243 (28/32 cells, Figure 5C2, bottom, chi-square test, p=0.03). These results demonstrate a significant difference
244 in the proportion of MD cells showing a late synaptic response between WT and Shank3$^{-/-}$ mice at both P14
245 and adulthood. In adulthood, the persistent current build-up become greater in Shank3$^{-/-}$ mice than in WT
246 mice (Figure 5C4, bottom; WT vs. Shank3$^{-/-}$, 2-way ANOVA with repeated measures: genotype p=0.02;
247 stimulation p<0.0001; interaction p<0.0001).

248 We found that upon termination of oEPSC trains, MD neurons additionally displayed a slowly-decaying
249 "residual" response lasting for several seconds, much longer than the decay time constant of individual
250 oEPSCs reported above (<50 ms). We quantified the residual current as that measured 500 ms following
251 the end of the stimulus train and found that it was greater in Shank3$^{-/-}$ mice, but only in adults (Figure 5C5;
252 mean ± sem; P14: WT=-3.5 ± 5.6; Shank3–/– = -7.9 ± 8.8; Mann-Whitney test, p=0.1; adult: WT = -12.2 ±
253 3.2; Shank3$^{-/-}$ = -22.8 ± 4.1, Mann-Whitney test, p=0.002).

254 These findings indicate increases in connection strength between mPFC and MD neurons in Shank3$^{-/-}$ mice.
255 This synaptic strengthening becomes especially evident during repetitive activation with 10 Hz stimulus
256 trains. This then triggers to greater recruitment of MD cells as measured by numbers of evoked action
257 potentials (Figure 5D1-3, WT vs Shank3$^{-/-}$, 2-way ANOVA with repeated measures, P14: genotype p=0.02;
258 stimulation p=0.2; interaction p=0.9; adult: genotype p=0.049, stimulation p<0.0001, interaction p=0.0001).

259 **Synaptic receptors underlying the augmented function of the mPFC-MD synapse in Shank3$^{-/-}$ mice**

260 To investigate the nature of the persistent synaptic current in Shank3$^{-/-}$ mice, we conducted a set of separate
261 experiments using pharmacological compounds targeting two major receptor classes known to be affected
262 by Shank3 mutations in other brain regions. Additionally, we chose to target receptors with a long duration
263 of action, based on the previously observed increase in oEPSC decay time and the presence of late
264 persistent current in Shank3$^{-/-}$ mice (Figure 5). First, we used AP5, an antagonist of NMDA receptors.
265 Second, we conducted an occlusion experiment using DHPG, an agonist of mGluR1 and mGluR5 receptors.
266 These drugs were applied only if the recorded cell exhibited at least 10 pA of persistent current.

267 We first hypothesized that the increase in persistent current is mediated by NMDARs. Accordingly, bath
268 application of AP5 should induce little to no reduction in WT mice, as oEPSCs recorded at -70 mV are
269 predominantly mediated through AMPARs due to the magnesium block on NMDARs. Consistent with this,
270 0.1uM AP5 had no significant effect on phasic or persistent currents in WT mice. However, in Shank3$^{-/-}$
271 mice, AP5 reduced both phasic (Figure 6 A, B ;2 way-repeated ANOVA, bath vs AP5, drug p=0.009,
272 stimulation p=0.3, interaction p=0.9) and persistent current (Figure 6 A, C;2 way-repeated ANOVA, bath vs
273 AP5, drug p=0.0001, stimulation p<0.0001, interaction p<0.0001), indicating that the Shank3$^{-/-}$ mutation
274 results in abnormal functional activation of NMDARs.

275 Our second hypothesis, based on the original Shank3$^{-/-}$ complete knockout model(11), is that there is a
276 dysregulation of postsynaptic mGluR5 signaling, which might be expected given that mGluRs show long-
277 lasting responses(39) . We initially tried to use MTEP, the antagonist of mGluR5, but the results were
278 inconclusive. To further investigate, we performed an occlusion experiment using DHPG, a mGluR1 and
279 mGluR5 agonist, reasoning that this would reduce the amplitude of the synaptic response, as a subset of
280 post-synaptic mGluRs would already be activated by bound DHPG. We observed a decrease in both
281 persistent (Figure 6D, F; 2-way repeated ANOVA, bath vs. DHPG, drug p=0.003, stimulation p=0.7,
282 interaction p<0.0001) and phasic currents (Figure 6D, E; 2-way repeated ANOVA, bath vs. DHPG, drug
283 p=0.003, stimulation p=0.7, interaction p<0.0001) in Shank3$^{-/-}$ mice, but no change in WT mice. The lack of
284 effect in WT mice suggests that mGluR1/5 signaling is tightly regulated and not recruited at either pre- or
285 postsynaptic sites under normal conditions. In contrast, the reduction in phasic and persistent currents in
286 Shank3$^{-/-}$ mice upon DHPG application likely reflects a dysregulation of mGluR1/5 signaling.

287 **Discussion**

288 In this study, we investigated the pathophysiological development of the medial prefrontal cortex (mPFC)
289 and its output to the mediodorsal thalamus using the Shank3$^{-/-}$ mouse model of autism spectrum disorder
290 (ASD). After initially assessing function at P11, we mainly compared relevant developmental time points,
291 specifically P14 (pre-weaning stage) and adulthood (>P55). Initially, we confirmed known ASD-related
292 behavioral deficits, including impaired social behaviors in adult mice and altered ultrasonic vocalizations
293 (USVs) in juvenile mice. We then employed our in vitro local field potential (LFP) recording design, which
294 allowed us to identify a significant difference between the P14 and adult stages. At P14, we observed
295 hypoexcitability, with a switch to mPFC circuit hyperfunction in adults. Furthermore, using whole-cell patch-

clamp recordings of pyramidal cells, we uncovered distinct developmental patterns between cortical layers: at P14, layer 2/3 pyramidal cells exhibited hypoexcitability, while layer 5 cells showed signs of hyperexcitability. As the mice matured, the hyperexcitability in layer 5 cells was exacerbated, whereas layer 2/3 cells tended to normalize their excitability. Interestingly, we observed that the excitation/inhibition (E/I) ratio was altered specifically in layer 5 neurons at both developmental stages, while no significant changes were observed in layer 2/3 cells. These findings led us to further investigate the mPFC-mediodorsal (MD) thalamus pathway, a major connection dependent on layer 5 output and involved in social behavior. We observed significant alterations in this pathway, with changes in synaptic strength and post-synaptic receptor composition in Shank3$^{-/-}$ mice, which were linked to disruptions in NMDA and mGluR group 1 receptor signaling.

Longitudinal approaches in ASD research

While much ASD research focuses on mature animals, longitudinal studies are critical for understanding how genetic mutations influence neurodevelopment. Our study highlights the progression of deficits in Shank3$^{-/-}$ mice, starting with early behavioral alterations at P11 and cellular hypoexcitability at P14, which then evolves into circuit hyperfunction in adulthood. The observed shift in mPFC network activity across development, from hypoexcitability to hyperfunction, is to our knowledge a completely novel finding. Observations of early cellular deficits have been reported in other studies using a different Shank3 mutant model, Shank3B$^{-/-}$, in the corticostriatal circuit, where early abnormal hyperactivity of corticostriatal afferents was observed(40), however the long-term changes into adulthood were not reported. This group also confirmed early behavioral alterations in the Shank3B$^{-/-}$ model(41). Altered USVs are also commonly observed in various genetic mouse models of ASD(10). These observations suggest that longitudinal approaches, such as our work, can provide critical insights into how gene mutations influence the progression of ASD over time and might help reveal potential targets and windows for therapeutic intervention.

Layer-Specific mPFC Excitability in ASD

As mentioned above we found layer specific mPFC deficits that are different at P14 compared to the adults. The scientific literature regarding mPFC dysfunction has largely focused on mature animals(5,23,42,43). The hyperexcitability observed in mPFC layer 5 pyramidal cells is consistent with findings in other mouse model(5,35,44). However, other reports suggest that mPFC layer 2/3 cells can be altered in genetic mouse ASD models(30,43). Our intracellular recording data (Figure 3) revealed that while the intrinsic properties of layer 2/3 pyramidal cells are comparable between adult Shank3$^{-/-}$ and WT mice, layer 5 pyramidal cells exhibit hyperexcitability in Shank3$^{-/-}$ mice. A novel finding of our study is that these properties appear to be dynamic and development-dependent. Specifically, we detected hypoexcitability in layer 2/3 cells at P14, while layer 5 cells exhibited only a mild hyperexcitability—characterized by a depolarized resting membrane potential—at this stage. We speculate that compensatory mechanisms may normalize layer 2/3 cell excitability by adulthood, while at the same time this could, through enhanced output, lead to

332 hyperexcitability in layer 5 cells in adult mice. Pyramidal cell morphology and intrinsic membrane properties
333 develop in parallel in layers 2/3 and 5; however, the development of synaptic inputs differs between these
334 layers(45) : during the first two postnatal weeks, layer 2/3 primarily receives excitatory inputs, while layer 5
335 does not(46). Shank3 is a scaffolding protein found in excitatory synapses(47,48). Its knockout may first
336 affect early-developing synapses in layer 2/3 before impacting those in layer 5. This suggests that different
337 layers of the mPFC may be affected differently to different ASD- related gene mutations.

338 Taking advantage of simultaneous recordings across layers with our in vitro multi-electrode array assay
339 (Figure 2), we recorded LFP/CSD signals reflecting synaptic activity in mPFC neurons. Comparable to our
340 patch-clamp data, we observed an interesting dynamic of signal excitability depending on age. At P14, we
341 discovered that only the presynaptic signal (fiber volley) in layer 5 is hypoexcitable. This signal is likely
342 dominated by thalamic inputs to the mPFC. In adulthood, we observed a global presynaptic hyperfunction
343 of the mPFC across both layers, with layer 5 postsynaptic signals also hyperfunctional. Our results highlight
344 the heterogeneity of ASD-related neurodevelopmental changes, where distinct mPFC layers and synaptic
345 circuits exhibit alterations at different developmental stages. Consequently, these findings underscore the
346 importance of considering both layer-specific and age-dependent parameters when studying the
347 pathophysiological mechanisms linked to ASD.

348 **E/I ratio theory in ASD**

349 Twenty years ago, Rubenstein and Merzenich hypothesized that ASD dysfunction may generally be related
350 to increase in excitatory/ inhibitory ratio(38). This theory has been of interest of many(8,49) as it can relate
351 to different ASD mouse models. Recently, Antoine et al. (50) has observed an elevated E-I ratio is a common
352 circuit phenotype in four different genetic mouse models of ASD. They demonstrated that this elevation
353 reflects stabilization of synaptic drive rather than driving network hyperexcitability, as was previously
354 believed. In contrast, in our study (Figure 4), we observed a reduction in the E/I ratio in Shank3$^{-/-}$ mPFC
355 layer 5 cells at both P14 and in adults. Despite this, LFP recordings revealed global mPFC hyperfunction
356 and layer 5 pyramidal neuron hyperexcitability in adults, though less so at P14. These results do not directly
357 contradict the findings of Antoine et al. but suggest that the E/I ratio imbalance as observed at the single
358 cell level may not necessarily be the cause of the observed network excitability changes. Instead, the
359 reduced E/I ratio we observed may reflect an adaptive response to early cellular-level disruptions, possibly
360 originating from developmental imbalances that influence network function later. Additionally, at this point
361 we cannot exclude potential changes in interneuron excitability, as Shank3$^{-/-}$ models have been shown to
362 exhibit deficits in interneuron function, which could also contribute to the observed network
363 alterations(51,52).

364 **mPFC-MD synaptic connectivity**

365 Both P14 and adult Shank3$^{-/-}$ mice exhibit altered mPFC-MD thalamus synaptic connectivity which results
366 in a functional increase in mPFC-driven MD neuron spikes (Figure 5). Additionally, we observed a greater

incidence of persistent and residual synaptic responses in MD neurons of adult Shank3$^{-/-}$ mice which may contribute to behavioral dysfunction. In agreement with our observation of altered corticothalamic connectivity, it has been shown that sensory cortico-thalamic synapses are also altered in adults Shank3$^{-/-}$ mice(53), also displaying a buildup of current under a 40Hz train stimulation.

Clues for a critical period of development for the mPFC-MD circuit have emerged. Indeed, anatomical lesions(54) or chemogenetic modulation to disturb the mPFC-MD circuit before adulthood results in physiological changes of mPFC activity(55,56) or social behavior(55). Similar modulation in adulthood failed to affect mPFC circuits or social behavioral changes. It is interesting to note that the density of connections between the mPFC and MD regions decreases at postnatal day 14 (P14)(12) and that a similar decrease in the expression of the SHANK3 transcript occurs at the same time point(18). Our findings emphasize significant alterations in mPFC-MD synaptic connectivity in Shank3$^{-/-}$ mice, with functional changes evident across both juvenile and adult stages. The increased incidence of persistent synaptic responses in adult mice underscores the lasting impact of these early disruptions, highlighting the need to further understand how such changes contribute to behavioral dysfunction.

Importantly, the choice of NMDA and mGluR pharmacological manipulations was motivated by the longer decay times observed in MD cells of Shank3$^{-/-}$ mice (Figure 6). This observation led to several mechanistic hypotheses, including receptor mislocalization(11), spillover effects(57), altered receptor composition(58,59), or an incomplete developmental switch(60). Interestingly, pharmacological modulation affected the persistent component in Shank3$^{-/-}$ mice but had no detectable impact on WT, suggesting that NMDARs and mGluRs are indeed potential targets for this buildup of current in Shank3$^{-/-}$ mice. In our study, we observed a novel population difference in the presence of persistent currents between Shank3$^{-/-}$ and WT mice. Specifically, at both P14 and in adults, a majority of cells with from Shank3 mutants showed persistent currents, whereas WT mice displayed a higher proportion of cells with persistent currents at P14 (70%) and a reduced proportion in adults (35%) (Figure 5). This finding is consistent with the known alterations in NMDA receptor-mediated neurotransmission in other Shank3 loss of function models(55,61), where NMDA signaling is disrupted. Additionally, the occlusion experiment with DHPG provided further insight into the altered receptor signaling in Shank3$^{-/-}$ mice. DHPG application led to also to a reduction in phasic current, suggesting that presynaptic alterations could contribute to the phenotype. Collectively, these findings reinforce the notion that Shank3 deficiency leads to disruptions in both NMDA and mGluR1/5 signaling pathways, ultimately affecting synaptic transmission.

Caveats and limitations

Here we demonstrated novel findings of developmental ASD-related circuit dysfunction in a model of severe ASD, Shank3$^{-/-}$ mice, at two important time points: P14 and adults (>P55). However, a potential limitation of our results is that they were mainly obtained in isolated brain slices. These have the advantage of being accessible for mechanistic and pharmacological characterization, using LFP or cellular physiology. However, the conditions *in vitro* can never completely match those in the intact brain, and any disease-related

differences in extrinsic connectivity, neuromodulatory state, etc. will not be directly revealed by the in vitro approach. Yet the use of in vitro optogenetics and pharmacology has the advantage of leading to better understanding of cellular/molecular pathophysiological mechanisms directly related to genetic mutations. One additional potential drawback of LFP network analysis is that the mode of synaptic stimulation is through single extracellular stimulus pulse that evokes a simplified and highly synchronized input that may not model normal ongoing circuit activity in behaving animals. Yet being able to reliably and quantitatively determine input-output relationships provides an integrated and robust assay of circuit excitability and E/I ratio that together outweigh this limitation. Further, given that both WT and Shank3$^{-/-}$ slices received comparable stimulation, yet displayed different responses, with hyperfunction of mPFC observed in adult Shank3$^{-/-}$, it indicates that the circuit state in Shank3$^{-/-}$ is more sensitive to synaptic input than in the WT. It would be interesting in the future to perform similar experiments *in vivo* by for example optogenetically stimulating the MD thalamus axon in mPFC while recording mPFC activity with linear silicon multielectrode probes. Another limitation of our study is that as of now, there is no direct evidence of a link between early circuit dysfunction and later behavioral effects. Future studies, using in vivo recording, like fiberphotometry(62) or miniscope(25) during the social interaction task will allow to relate the activity of mPFC (bulk fiberphotometry signal) or mPFC cells (miniscope) to the deficits. Finally, our study can be a starting point for establishing a causal link between early neurodevelopmental events and ASD-relevant neural circuit alterations. Acute mPFC circuit manipulation using optogenetics(62) or chemogenetics(55,63) in adults has been shown to be able to rescue some social behavior. It will be interesting to see if similar manipulations performed chronically during early life will have a significant impact on adult physiology and behavior. By identifying these critical periods of mPFC development, we might be able to perform early interventions that may prevent or mitigate ASD-related circuit dysfunction.

Conclusions and future directions

This study uncovers a critical and never described shift in mPFC network activity in Shank3$^{-/-}$ mice with distinct layer-specific alterations. Our findings highlight the progressive nature of ASD-related cortical dysfunction, emphasizing disruptions in the mPFC-mediodorsal thalamus pathway as a potential link to behavioral deficits. Crucially, this research underscores the importance of developmental timing in ASD, suggesting that early circuit dysfunction may set the stage for long-term impairments. By identifying these critical windows, our work lays the foundation for targeted early interventions, opening new possibilities for mitigating ASD-related neurodevelopmental disruptions.

Materials and Methods

Animals

Mice were bred and maintained according to Stanford University, School of Medicine Animal Research Requirements, and all procedures were approved by the Committees on Animal Research at Stanford University (protocol number: 12363). Mice carrying the *Shank3* complete knock out (Δe4–22) were a kind

438 gift from Dr. Yong-Hui Jiang(11), Duke University. All comparisons were made using both genders. Mice
439 used for experiments were separated in two distinct age group: P14 (+/- ½ day) and adults (2-4 months).
440 The mice were maintained on a 12 hr light/dark cycle. Food and water were available ad libitum.

441 **Genotyping of transgenic animals**

442 Shank3$^{-/-}$ and Shank3 WT mice were genotyped by PCR using the following primers: wild-type forward
443 GTGCCACGATCTTCCTCTAAAC, wild-type reverse, AGCTGGAGCGAGATAAGTATGC, mutant forward
444 TTGCATCTGGGACCTACTCC and mutant reverse AAAGCACTGACTCCTCTCTTGG.

445 **Behavioral tests**

446 *Ultrasonic vocalization recordings*

447 Ultrasonic vocalizations are typically emitted by pups from birth to the weaning period and are related to
448 communication behavior. In this study, we elicited ultrasonic vocalizations (USVs) by isolating the pups
449 briefly from their dams and littermates(64). Specifically, one hour before the recordings, on postnatal day 11
450 (P11) the breeders were removed from the home cage. The home cage with the remaining litter was then
451 moved to the testing room and placed on a heating pad for one hour to maintain the body temperature.
452 Pups were then individually isolated. Each tested pup was placed in a testing cage within a sound-isolated,
453 darkened box, with an UltraSoundGate 116Unb recording system (Avisoft Bioacoustics) positioned 15 to 20
454 cm above. The USVs were recorded with a sampling rate of 384,000 Hz in a 16-bit format (recording range:
455 0-250 kHz) for 10 minutes using the Avisoft-RECORDER USG/USGH software. Finally, the pup was
456 returned to its home cage with its littermates. Once the entire litter had been tested, the home cage was
457 returned to its original room, and the breeders were placed back in the cage. The recordings were next
458 analyzed using the Avisoft-SASLab Pro software (version 5.3.2-14; Avisoft Bioacoustics). In recordings of
459 pup vocalizations over a 10-minute period, the first 2 minutes are excluded from analysis as the calls may
460 result from handling-related stress. Fourier transformation (512pt FFT, Frame=100%, Hamming window with
461 75% of time overlap) was applied to obtain the spectrograms (500Hz: Frequency resolution; 0.5ms: Time
462 resolution). USV detection was performed using automatic whistle tracking in SASLab. Monotonic calls with
463 a minimal duration of 5 ms and slope of -15 to 6kHz/ms were counted. Number of calls was tested for
464 Normality using a Shapiro-Wilk test. Between-group comparison was performed using a non-parametric
465 Mann Whitney test. Data are reported as mean+/- sem.

466 *Social preference test*

467 To measure sociability, mice were tested in a social interaction task. A clean box was partitioned into three
468 zones. A camera was mounted directly above the box to record videos that were analyzed offline. Tested
469 mice were habituated to the empty box for ten minutes, the first day. The next day, a pre-test phase was

470 performed using two empty cages, one at each end of the box. The tested mouse had 10 minutes to explore.
471 The test phase is performed 10 minutes later. A novel object was placed within a perforated cage at one
472 end of the box and a conspecific is placed in a cage at the opposite end. The placement of the novel object
473 and never-met mouse was randomly assigned. Using EzTrack(65), the videos were scored to determine
474 mouse position, including time spent in regions of interest (ROIs) drawn around the cage containing either
475 the novel object or the conspecific. After checking for normality, the interaction time between an inanimate
476 object or conspecific was tested using a Welch's t-test.

477 **Extracellular multielectrode recordings**

478 Extracellular recordings were performed on coronal neocortical 400 µm thick slices from P14 or adults
479 (>P55) Shank3$^{-/-}$or Shank3 wild type (WT) containing the medial prefrontal cortex (mPFC). Slices were
480 recorded in a humidified oxygenated interface chamber at 34°C and perfused at a rate of 2 ml/min with
481 oxygenated artificial cerebrospinal fluid (aCSF). The aCSF contained (in mM): 10 glucose, 26 $NaHCO_3$, 2.5
482 KCl, 1.25 $NaHPO_4$, 1 $MgSO_4$, 2 $CaCl_2$, and 126 NaCl (300 mOsm).
483 A linear silicon multichannel probe (16 channels, 100 µm inter-electrode spacing, NeuroNexus
484 Technologies) was positioned normal to the medial surface and spanning across all layers of the mPFC to
485 record evoked local field potentials (LFPs). The silicon probe was linked to a pre-amplifier (PZ5-32, Tucker-
486 Davis Technologies (TDT)), and recordings were made using an RZ5D processor (TDT). Data acquisition
487 was conducted using the Real-time Processor Visual Design Studio (RPvdsEx) tool and a custom Python
488 code. LFP data were acquired at 25 kHz and filtered between 0.1 and 500 Hz. A bipolar tungsten
489 microelectrode (each wire, 50-100 kΩ, FHC) positioned in upper layer 5 was used to deliver a bipolar
490 electrical stimulation (0.1ms duration, intensity loops from 100 to 800 µA, interval of 15s). In order to obtain
491 a more reliable index of the location, direction, and magnitude of currents underlying network activity, we
492 derived the current-source density (CSD) from raw LFP signals(26). Assuming a uniform extracellular
493 resistivity, the CSD can be estimated as the second spatial derivative of the LFP. In our experiment, CSD
494 was computed in mPFC by algebraic differentiation of the LFP at adjacent electrodes in the linear probe
495 spaced by 100µm and assumed a uniform extracellular resistivity of 0.3 S/m(66). In addition, the following
496 drugs, DNQX (AMPAR antagonist; 25uM) and CPPene (SDZ EAA 494; NMDA competitive antagonist; 1µM)
497 were applied in the bath to identify the pre and post synaptic component of our signals. Relevant
498 components were next identified based on their distinct shape and their amplitude was measured for each
499 slice. Between-group comparison was performed using a 2-way repeated measure ANOVA. Data are
500 reported as mean+/- sem.

501 **Electrophysiological whole-cell patch-clamp recordings in mPFC slices**

502 Mice were deeply anesthetized with isoflurane (for P14 mice) or pentobarbital sodium (i.p., 50mg/kg; for
503 adult mice). P14 mice were directly decapitated. Adult mice were perfused transcardially with ice-cold (4ºC),
504 oxygenated (95% O_2 /5% CO_2) sucrose slicing solution containing (in mM): 234 sucrose, 11 glucose, 26

505 $NaHCO_3$, 2.5 KCl, 1.25 NaH_2PO_4, 10 $MgSO_4$, and 0.5 $CaCl_2$ (310 mOsm). Brains were quickly removed and
506 250 µm-thick coronal slices of mPFC cortex were cut in sucrose ACSF using a vibratome (VT1200; Leica).
507 Slices were transferred to a holding chamber filled with standard ACSF bubbled with 95% O_2 and 5% CO_2.
508 The composition of aCSF was (in mM): 10 glucose, 26 $NaHCO_3$, 2.5 KCl, 1.25 $NaHPO_4$, 1 $MgSO_4$, 2 $CaCl_2$,
509 and 126 NaCl (300 mOsm). Slices were allowed to recover 30 minutes at 37°C and were then incubated at
510 room temperature (20–25°C) until recording.

511 Individual slices were transferred to a recording chamber and continuously perfused at 2ml/min with
512 oxygenated aCSF at room temperature. Patch pipettes (3-5 MΩ) were pulled from borosilicate glass (Sutter
513 Instrument, CA, USA) on a micropipette puller (Model P1000, Sutter Instrument, CA, USA) and filled with
514 an intracellular solution containing (in mM): K-gluconate, 144; $MgCl_2$, 3; HEPES, 10; EGTA, 0.5 and 2 mg/ml
515 biocytin, pH= 7.2, 280mOsm. Whole-cell patch-clamp recordings were obtained from layer 2/3 or layer 5
516 pyramidal cells selected based on their morphology and electrophysiological profile. Recordings were
517 performed at room temperature (20–25°C) using a patch-clamp amplifier (Multiclamp 700B, Molecular
518 Devices) connected to a Digidata 1440A interface board (Molecular Devices). Signals were amplified and
519 collected using pClamp 10.7. Cells with an a stable access resistance of <25MΩ were analyzed. Resting
520 membrane potential was measured immediately upon obtaining the whole-cell configuration, and only cells
521 with a resting membrane potential more hyperpolarized than −50 mV were selected. Resting membrane
522 potential was computed as the average of the sweeps were no current was injected. Membrane potentials
523 were not corrected for junction potential. Cells were held at their resting membrane potential and V/I curves
524 were constructed from a series of current steps in 10pA and 20pA increments. Input resistance was
525 determined from the slope of the V/I curve in the linear region within 5 mV of the resting membrane potential.
526 Rheobase was calculated as the minimal depolarizing current step triggering an action potential. A tungsten
527 bipolar stimulating electrode was placed in mPFC layer 2-3 to evoke synaptic responses. Cells were held
528 at -70mV to record excitatory synaptic current and with the same stimulus intensity at +10 mV to record the
529 inhibitory synaptic current. The peak amplitude of these excitatory and inhibitory evoked responses was
530 used to calculate the excitatory-inhibitory ratio. Results are given as mean ± standard error of the mean
531 (sem). Between-group comparisons were performed using parametric test. A p-value below 0.05 was
532 considered statistically significant.

533 After recordings, slices were fixed overnight at 4°C in 4% paraformaldehyde/ PBS and then washed in PBS.
534 Slices were processed using Alexafluor 488-conjugated streptavidin (1:500, Invitrogen) to reveal biocytin.
535 After a series of wash in PBS, slices were mounted on gelatin-coated slides in Fluoromount-G for confocal
536 microscopy.

537 **Morphological analysis**

538 Zeiss LSM900 laser scanning confocal microscope was used to image the mPFC layer 5 biocytin labelled
539 neurons with 63x objectives and a 488nm laser. Images were processed using ImageJ (National Institutes

540 of Health; http://rsbweb.nih.gov/ij/). Neuronal tracing and analysis were performed using the SNT
541 toolbox(67).

542

543 **Viral injections**

544 For adult experiments, the procedure for viral injection has been described in detail(68). Briefly, young adult
545 mice were anesthetized using isoflurane (3% induction, 1.5% maintenance) and received carprofen 5 mg/kg
546 intra peritoneal injection. Mice received bilateral injection in mPFC (in mm from bregma, AP 1.8, ML +/-0.5,
547 DV -2.6). A volume of 500nl of virus encoding the ChR2 (AAV1-CaMKIIa-ChR2(H134R)_eYFP-WPRE-HGH,
548 10^{12} GC, 100 nl/min, Penn Vector Core, Addgene 26969P) was delivered to the injection sites.

549 For P14 recordings, P0 mice were anesthetized on ice. Mice received a bilateral injection in the frontal area
550 (in mm from lambda, AP: 3.5, ML:+/-0.1, DV:-1.5). A volume from 100 to 200nl of virus encoding the ChR2
551 (AAVDJ-CaMKIIa-ChR2(H134R)_eYFP, 10^{12} GC, 100 nl/min, Gene Vector and Virus Core at Stanford
552 University, catalog #36) was delivered to the injection sites.

553 **Optogenetics experiments**

554 ChR2-expressing mPFC axons to MD thalamus neurons were activated using blue LEDs stimulations
555 (Thorlabs M450LP2, 450 nm, duration 1 ms, maximal light intensity 13 mW, 19 mW/cm2) or blue laser
556 (Laserglow Technologies, 473 nm, duration 1 ms, maximal light intensity 8 mW, 10.8 mW/cm2). The mPFC-
557 MD thalamus synaptic connection was evaluated using 10 light stimulations at both 1Hz and 10Hz, with one
558 train administered every 20 seconds, while maintaining voltage clamp at -70mV. The resultant synaptic
559 responses were evaluated in voltage clamp to measure synaptic current and in current clamp to quantify
560 the number of action potentials. Synaptic properties parameters were measured using custom MATLAB
561 code.

562 To investigate the receptor composition underlying the abnormal persistent current observed in adult
563 Shank3$^{-/-}$ mutant mice, either DL-2-Amino-5-phosphonovaleric acid (AP5, Sigma, A5282) at a concentration
564 of 100 μM (broad-spectrum NMDA receptor blocker) or (RS)-3,5-Dihydroxyphenylglycine (DHPG, Tocris,
565 #0342) at a concentration of 10 μM (selective group I mGluR agonist) were applied for 10 minutes in the
566 bath after obtaining a stable baseline recording. Partial washout was obtained in some cases. The impact
567 of AP5 and DHPG on the 10Hz voltage-clamp synaptic response was quantified and compared to the
568 baseline recordings. Statistical analysis, 2-way ANOVA with repeated measure, was performed to evaluate
569 the significance of the effects observed.

570

571 ## Acknowledgments

572 We thank all past and current lab members for their valuable feedback throughout this project. We are
573 grateful to Katlin Villar, Cameron Glick, and Nicole Agranonik for their assistance in managing mouse lines,

574 laboratory equipment, and supplies. We also thank Laura Denardo and Rui Peixoto and their team for their
575 invaluable advice on P0 virus injections.

576 **Funding sources**

577 This work was supported by SFARI award # 633450, Screening for convergence of axonal dysfunction
578 across diverse mouse models of autism.

579 **References**

580 1. Wetherby AM, Woods J, Allen L, Cleary J, Dickinson H, Lord C. Early Indicators of Autism Spectrum
581 Disorders in the Second Year of Life. J Autism Dev Disord. 2004 Oct 1;34(5):473–93.

582 2. De Giacomo A, Fombonne E. Parental recognition of developmental abnormalities in autism.
583 European Child & Adolescent Psychiatry. 1998 Oct 1;7(3):131–6.

584 3. Hodel AS. Rapid infant prefrontal cortex development and sensitivity to early environmental
585 experience. Developmental Review. 2018 Jun 1;48:113–44.

586 4. Sato M, Nakai N, Fujima S, Choe KY, Takumi T. Social circuits and their dysfunction in autism
587 spectrum disorder. Molecular Psychiatry. 2023 Aug 1;28(8):3194–206.

588 5. Brumback AC, Ellwood IT, Kjaerby C, Iafrati J, Robinson S, Lee AT, et al. Identifying specific prefrontal
589 neurons that contribute to autism-associated abnormalities in physiology and social behavior. Mol
590 Psychiatry. 2018 Oct;23(10):2078–89.

591 6. Luo Y, Wang L, Cao Y, Shen Y, Gu Y, Wang L. Reduced excitatory activity in the developing mPFC
592 mediates a PVH-to-PVL transition and impaired social cognition in autism spectrum disorders. Transl
593 Psychiatry. 2024 Aug 6;14(1):1–14.

594 7. Amodio DM, Frith CD. Meeting of minds: the medial frontal cortex and social cognition. Nat Rev
595 Neurosci. 2006 Apr;7(4):268–77.

596 8. Yizhar O, Fenno LE, Prigge M, Schneider F, Davidson TJ, O'Shea DJ, et al. Neocortical
597 excitation/inhibition balance in information processing and social dysfunction. Nature. 2011
598 Sep;477(7363):171–8.

599 9. Lee E, Rhim I, Lee JW, Ghim JW, Lee S, Kim E, et al. Enhanced Neuronal Activity in the Medial
600 Prefrontal Cortex during Social Approach Behavior. J Neurosci. 2016 Jun 29;36(26):6926–36.

601 10. Lai JKY, Sobala-Drozdowski M, Zhou L, Doering LC, Faure PA, Foster JA. Temporal and spectral
602 differences in the ultrasonic vocalizations of fragile X knock out mice during postnatal development.
603 Behav Brain Res. 2014 Feb 1;259:119–30.

604 11. Wang X, Bey AL, Katz BM, Badea A, Kim N, David LK, et al. Altered mGluR5-Homer scaffolds and
605 corticostriatal connectivity in a Shank3 complete knockout model of autism. Nat Commun. 2016 May
606 10;7:11459.

607 12. Klune CB, Jin B, DeNardo LA. Linking mPFC circuit maturation to the developmental regulation of
608 emotional memory and cognitive flexibility. eLife. 2021 May 5;10:e64567.

609 13. Kolk SM, Rakic P. Development of prefrontal cortex. Neuropsychopharmacol. 2022 Jan;47(1):41–57.

610 14. Ferguson BR, Gao WJ. Development of thalamocortical connections between the mediodorsal
611 thalamus and the prefrontal cortex and its implication in cognition. Front Hum Neurosci [Internet].
612 2015 Jan 9 [cited 2023 Feb 9];8. Available from:
613 http://journal.frontiersin.org/article/10.3389/fnhum.2014.01027/abstract

614 15. Verpelli C, Dvoretskova E, Vicidomini C, Rossi F, Chiappalone M, Schoen M, et al. Importance of
615 Shank3 protein in regulating metabotropic glutamate receptor 5 (mGluR5) expression and signaling at
616 synapses. J Biol Chem. 2011 Oct 7;286(40):34839–50.

617 16. Moessner R, Marshall CR, Sutcliffe JS, Skaug J, Pinto D, Vincent J, et al. Contribution of SHANK3
618 mutations to autism spectrum disorder. Am J Hum Genet. 2007 Dec;81(6):1289–97.

619 17. Boccuto L, Lauri M, Sarasua SM, Skinner CD, Buccella D, Dwivedi A, et al. Prevalence of SHANK3
620 variants in patients with different subtypes of autism spectrum disorders. Eur J Hum Genet. 2013
621 Mar;21(3):310–6.

622 18. Waga C, Asano H, Sanagi T, Suzuki E, Nakamura Y, Tsuchiya A, et al. Identification of two novel
623 *Shank3* transcripts in the developing mouse neocortex. J Neurochem. 2014 Jan;128(2):280–93.

624 19. Rios O, Villalobos J. Postnatal development of the afferent projections from the dorsomedial thalamic
625 nucleus to the frontal cortex in mice. Developmental Brain Research. 2004 May 19;150(1):47–50.

626 20. Peça J, Feliciano C, Ting JT, Wang W, Wells MF, Venkatraman TN, et al. Shank3 mutant mice display
627 autistic-like behaviours and striatal dysfunction. Nature. 2011 Apr 28;472(7344):437–42.

628 21. Caruso A, Marconi MA, Scattoni ML, Ricceri L. Ultrasonic vocalizations in laboratory mice: strain, age,
629 and sex differences. Genes Brain Behav. 2022 Jun 10;21(5):e12815.

630 22. Kalinowska M, van der Lei MB, Kitiashvili M, Mamcarz M, Oliveira MM, Longo F, et al. Deletion of
631 Fmr1 in parvalbumin-expressing neurons results in dysregulated translation and selective behavioral
632 deficits associated with fragile X syndrome. Molecular Autism. 2022 Jun 29;13(1):29.

633 23. Jang WE, Park JH, Park G, Bang G, Na CH, Kim JY, et al. Cntnap2-dependent molecular networks in
634 autism spectrum disorder revealed through an integrative multi-omics analysis. Mol Psychiatry. 2023
635 Feb;28(2):810–21.

636 24. Tripathi MK, Ojha SK, Kartawy M, Khaliulin I, Hamoudi W, Amal H. Mutations associated with autism
637 lead to similar synaptic and behavioral alterations in both sexes of male and female mouse brain. Sci
638 Rep. 2024 Jan 4;14(1):10.

639 25. Liang B, Zhang L, Barbera G, Fang W, Zhang J, Chen X, et al. Distinct and Dynamic ON and OFF
640 Neural Ensembles in the Prefrontal Cortex Code Social Exploration. Neuron. 2018 Nov 7;100(3):700-
641 714.e9.

642 26. Nicholson C, Freeman JA. Theory of current source-density analysis and determination of
643 conductivity tensor for anuran cerebellum. J Neurophysiol. 1975 Mar;38(2):356–68.

644 27. Kumar SS, Huguenard JR. Properties of Excitatory Synaptic Connections Mediated by the Corpus
645 Callosum in the Developing Rat Neocortex. Journal of Neurophysiology. 2001 Dec;86(6):2973–85.

646 28. Douglas RJ, Koch C, Mahowald M, Martin KAC, Suarez HH. Recurrent Excitation in Neocortical
647 Circuits. Science. 1995 Aug 18;269(5226):981–5.

648 29. Kisvárday ZF, Martin KAC, Freund TF, Maglóczky Zs, Whitteridge D, Somogyi P. Synaptic targets of
649 HRP-filled layer III pyramidal cells in the cat striate cortex. Exp Brain Res. 1986 Nov 1;64(3):541–52.

30. Sacai H, Sakoori K, Konno K, Nagahama K, Suzuki H, Watanabe T, et al. Autism spectrum disorder-like behavior caused by reduced excitatory synaptic transmission in pyramidal neurons of mouse prefrontal cortex. Nat Commun. 2020 Oct 12;11(1):5140.

31. Anastasiades PG, Carter AG. Circuit organization of the rodent medial prefrontal cortex. Trends in Neurosciences. 2021 Jul;44(7):550–63.

32. Ferguson BR, Gao WJ. Thalamic Control of Cognition and Social Behavior Via Regulation of Gamma-Aminobutyric Acidergic Signaling and Excitation/Inhibition Balance in the Medial Prefrontal Cortex. Biological Psychiatry. 2018 Apr 15;83(8):657–69.

33. Ko J. Neuroanatomical Substrates of Rodent Social Behavior: The Medial Prefrontal Cortex and Its Projection Patterns. Front Neural Circuits [Internet]. 2017 Jun 13 [cited 2024 Sep 7];11. Available from: https://www.frontiersin.org/journals/neural-circuits/articles/10.3389/fncir.2017.00041/full

34. Testa-Silva G, Loebel A, Giugliano M, de Kock CPJ, Mansvelder HD, Meredith RM. Hyperconnectivity and Slow Synapses during Early Development of Medial Prefrontal Cortex in a Mouse Model for Mental Retardation and Autism. Cerebral Cortex. 2012 Jun;22(6):1333–42.

35. Pirone A, Alexander JM, Koenig JB, Cook-Snyder DR, Palnati M, Wickham RJ, et al. Social Stimulus Causes Aberrant Activation of the Medial Prefrontal Cortex in a Mouse Model With Autism-Like Behaviors. Front Synaptic Neurosci. 2018 Oct 12;10:35.

36. Lee AT, Gee SM, Vogt D, Patel T, Rubenstein JL, Sohal VS. Pyramidal Neurons in Prefrontal Cortex Receive Subtype-Specific Forms of Excitation and Inhibition. Neuron. 2014 Jan 8;81(1):61–8.

37. Ramaswamy S, Markram H. Anatomy and physiology of the thick-tufted layer 5 pyramidal neuron. Front Cell Neurosci. 2015 Jun 26;9:233.

38. Rubenstein JLR, Merzenich MM. Model of autism: increased ratio of excitation/inhibition in key neural systems. Genes Brain Behav. 2003 Oct;2(5):255–67.

39. Wong RKS, Chuang SC, Bianchi R. Metabotropic Glutamate Receptors and Epileptogenesis. Epilepsy Curr. 2002 May;2(3):81–5.

40. Peixoto RT, Wang W, Croney DM, Kozorovitskiy Y, Sabatini BL. Early hyperactivity and precocious maturation of corticostriatal circuits in Shank3B−/− mice. Nat Neurosci. 2016 May;19(5):716–24.

41. Peixoto RT, Chantranupong L, Hakim R, Levasseur J, Wang W, Merchant T, et al. Abnormal Striatal Development Underlies the Early Onset of Behavioral Deficits in Shank3B Mice. Cell Reports. 2019 Nov;29(7):2016-2027.e4.

42. Luo YF, Lu L, Song HY, Xu H, Zheng ZW, Wu ZY, et al. Divergent projections of the prelimbic cortex mediate autism- and anxiety-like behaviors. Mol Psychiatry. 2023 Jun;28(6):2343–54.

43. Lazaro MT, Taxidis J, Shuman T, Bachmutsky I, Ikrar T, Santos R, et al. Reduced Prefrontal Synaptic Connectivity and Disturbed Oscillatory Population Dynamics in the CNTNAP2 Model of Autism. Cell Reports. 2019 May;27(9):2567-2578.e6.

44. Kalmbach BE, Johnston D, Brager DH. Cell-Type Specific Channelopathies in the Prefrontal Cortex of the fmr1-/y Mouse Model of Fragile X Syndrome. eNeuro [Internet]. 2015 Nov 1 [cited 2024 Aug 30];2(6). Available from: https://www.eneuro.org/content/2/6/ENEURO.0114-15.2015

45. Brill J, Huguenard JR. Sequential changes in AMPA receptor targeting in the developing neocortical excitatory circuit. J Neurosci. 2008 Dec 17;28(51):13918–28.

690 46. Kroon T, van Hugte E, van Linge L, Mansvelder HD, Meredith RM. Early postnatal development of
691 pyramidal neurons across layers of the mouse medial prefrontal cortex. Sci Rep. 2019 Mar
692 25;9(1):5037.

693 47. Durand CM, Betancur C, Boeckers TM, Bockmann J, Chaste P, Fauchereau F, et al. Mutations in the
694 gene encoding the synaptic scaffolding protein SHANK3 are associated with autism spectrum
695 disorders. Nat Genet. 2007 Jan;39(1):25–7.

696 48. Ha HTT, Leal-Ortiz S, Lalwani K, Kiyonaka S, Hamachi I, Mysore SP, et al. Shank and Zinc Mediate
697 an AMPA Receptor Subunit Switch in Developing Neurons. Front Mol Neurosci [Internet]. 2018 Nov 9
698 [cited 2024 Sep 1];11. Available from: https://www.frontiersin.org/journals/molecular-
699 neuroscience/articles/10.3389/fnmol.2018.00405/full

700 49. Gogolla N, LeBlanc JJ, Quast KB, Südhof TC, Fagiolini M, Hensch TK. Common circuit defect of
701 excitatory-inhibitory balance in mouse models of autism. J Neurodevelop Disord. 2009 Jun
702 1;1(2):172–81.

703 50. Antoine MW, Langberg T, Schnepel P, Feldman DE. Increased Excitation-Inhibition Ratio Stabilizes
704 Synapse and Circuit Excitability in Four Autism Mouse Models. Neuron. 2019 Feb 20;101(4):648-
705 661.e4.

706 51. Shih YC, Nelson L, Janeček M, Peixoto RT. Late onset and regional heterogeneity of synaptic deficits
707 in cortical PV interneurons of Shank3B−/− mice [Internet]. bioRxiv; 2023 [cited 2024 Aug 8]. p.
708 2023.11.23.568500. Available from: https://www.biorxiv.org/content/10.1101/2023.11.23.568500v1

709 52. Chen Q, Deister CA, Gao X, Guo B, Lynn-Jones T, Chen N, et al. Dysfunction of cortical GABAergic
710 neurons leads to sensory hyper-reactivity in a Shank3 mouse model of ASD. Nat Neurosci. 2020
711 Apr;23(4):520–32.

712 53. Guo B, Liu T, Choi S, Mao H, Wang W, Xi K, et al. Restoring thalamocortical circuit dysfunction by
713 correcting HCN channelopathy in Shank3 mutant mice. CR Med [Internet]. 2024 May 21 [cited 2024
714 Sep 1];5(5). Available from: https://www.cell.com/cell-reports-medicine/abstract/S2666-
715 3791(24)00203-9

716 54. Marmolejo N, Paez J, Levitt JB, Jones LB. Early postnatal lesion of the medial dorsal nucleus leads to
717 loss of dendrites and spines in adult prefrontal cortex. Dev Neurosci. 2012;34(6):463–76.

718 55. Qin L, Ma K, Yan Z. Chemogenetic Activation of Prefrontal Cortex in Shank3-Deficient Mice
719 Ameliorates Social Deficits, NMDAR Hypofunction, and Sgk2 Downregulation. iScience. 2019
720 Jul;17:24–35.

721 56. Benoit LJ, Holt ES, Posani L, Fusi S, Harris AZ, Canetta S, et al. Adolescent thalamic inhibition leads
722 to long-lasting impairments in prefrontal cortex function. Nat Neurosci. 2022 Jun;25(6):714–25.

723 57. Venkatesan S, Binko MA, Mielnik CA, Ramsey AJ, Lambe EK. Deficits in integrative NMDA receptors
724 caused by Grin1 disruption can be rescued in adulthood. Neuropsychopharmacol. 2023
725 Nov;48(12):1742–51.

726 58. Fatemi SH, Folsom TD, Reutiman TJ, Thuras PD. Expression of GABAB receptors is altered in brains
727 of subjects with autism. Cerebellum. 2009 Mar;8(1):64–9.

728 59. Mejias R, Adamczyk A, Anggono V, Niranjan T, Thomas GM, Sharma K, et al. Gain-of-function
729 glutamate receptor interacting protein 1 variants alter GluA2 recycling and surface distribution in
730 patients with autism. Proc Natl Acad Sci U S A. 2011 Mar 22;108(12):4920–5.

731 60. Mangano GD, Riva A, Fontana A, Salpietro V, Mangano GR, Nobile G, et al. *De novo GRIN2A*
732 variants associated with epilepsy and autism and literature review. Epilepsy & Behavior. 2022 Apr
733 1;129:108604.

734 61. Duffney LJ, Wei J, Cheng J, Liu W, Smith KR, Kittler JT, et al. Shank3 Deficiency Induces NMDA
735 Receptor Hypofunction via an Actin-Dependent Mechanism. J Neurosci. 2013 Oct 2;33(40):15767–78.

736 62. Selimbeyoglu A, Kim CK, Inoue M, Lee SY, Hong ASO, Kauvar I, et al. Modulation of prefrontal cortex
737 excitation/inhibition balance rescues social behavior in *CNTNAP2* -deficient mice. Sci Transl Med.
738 2017 Aug 2;9(401):eaah6733.

739 63. Wang W, Rein B, Zhang F, Tan T, Zhong P, Qin L, et al. Chemogenetic Activation of Prefrontal Cortex
740 Rescues Synaptic and Behavioral Deficits in a Mouse Model of 16p11.2 Deletion Syndrome. J
741 Neurosci. 2018 Jun 27;38(26):5939–48.

742 64. Ultrasonic Vocalizations in Rat and Mouse Pups - Hofer - 2001 - Current Protocols in Neuroscience -
743 Wiley Online Library [Internet]. [cited 2024 Sep 8]. Available from:
744 https://currentprotocols.onlinelibrary.wiley.com/doi/abs/10.1002/0471142301.ns0814s17

745 65. Pennington ZT, Dong Z, Feng Y, Vetere LM, Page-Harley L, Shuman T, et al. ezTrack: An open-source
746 video analysis pipeline for the investigation of animal behavior. Sci Rep. 2019 Dec 27;9(1):19979.

747 66. Goto T, Hatanaka R, Ogawa T, Sumiyoshi A, Riera J, Kawashima R. An evaluation of the conductivity
748 profile in the somatosensory barrel cortex of Wistar rats. J Neurophysiol. 2010 Dec;104(6):3388–412.

749 67. Arshadi C, Günther U, Eddison M, Harrington KIS, Ferreira TA. SNT: a unifying toolbox for
750 quantification of neuronal anatomy. Nat Methods. 2021 Apr;18(4):374–7.

751 68. Vantomme G, Rovó Z, Cardis R, Béard E, Katsioudi G, Guadagno A, et al. A Thalamic Reticular
752 Circuit for Head Direction Cell Tuning and Spatial Navigation. Cell Rep. 2020 Jun 9;31(10):107747.

753

754

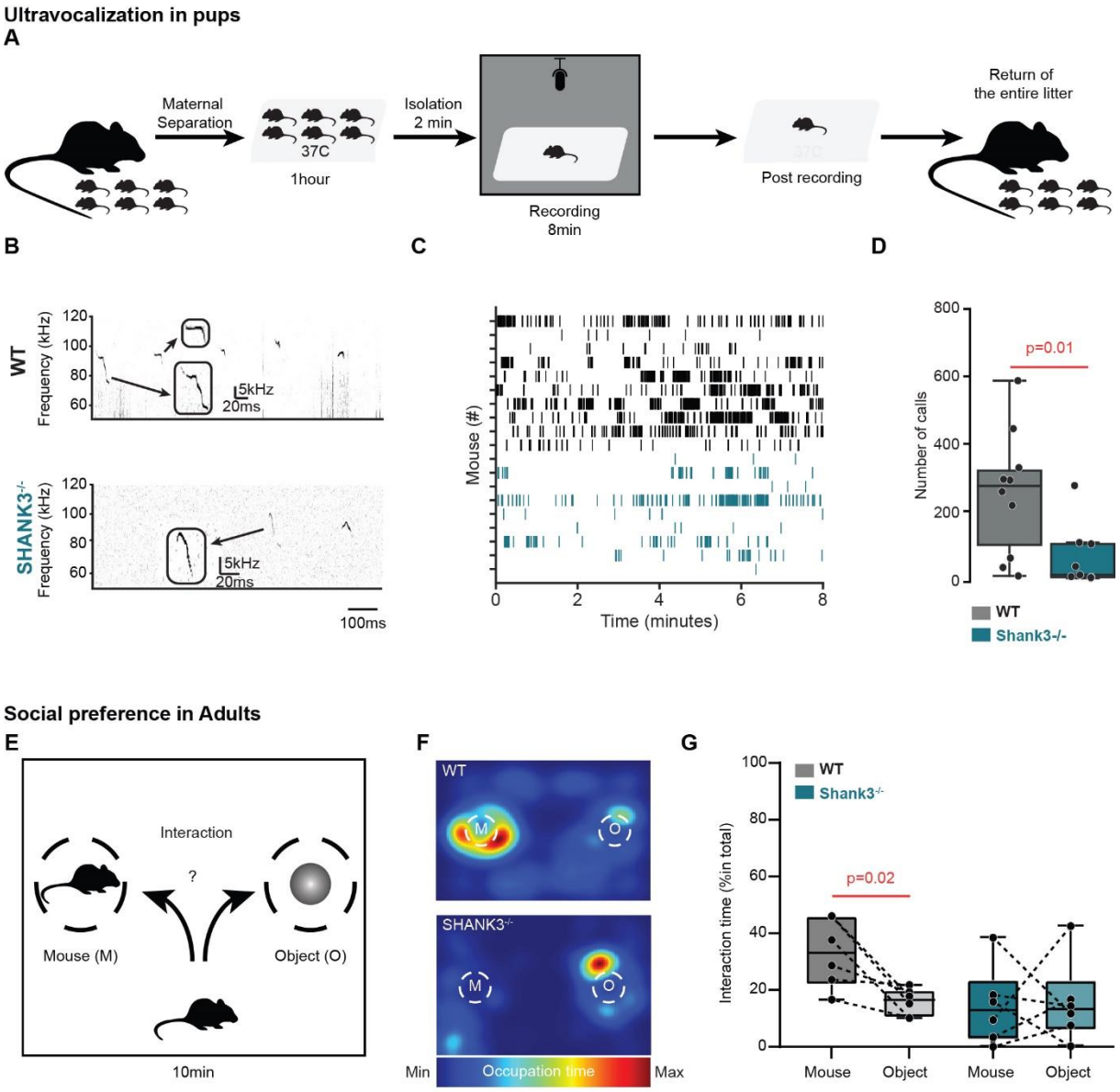

Figure 1. Shank3$^{-/-}$ mice display deficits in communication in early life and in social behavior in adulthood. (A) Schematic diagram of isolation and ultrasonic vocalization protocol performed in Shank3 WT and Shank3$^{-/-}$ P11 littermates. (B) Examples of 1 second long spectra (bottom images, in kHz) from USV recordings in WT and Shank3$^{-/-}$ mice. Insets show examples of individual syllables expanded as indicated by arrows in the original recordings. Left: WT (black); Right: Shank3 (blue). (C) Raster plot showing individual mouse ultrasonic vocalization (USV) calls during 8-minute recordings, with WT mice represented in black and Shank3$^{-/-}$ in blue (D) Number of calls for WT (grey) and Shank3$^{-/-}$ (blue). (E) Schematic diagram of social preference test performed in WT and Shank3$^{-/-}$ adults. (F) Example of occupation time heat maps for WT (top) and Shank3$^{-/-}$ (bottom) adults. (G) Percentage of the interaction time with a never-met conspecific (darker colors) or a novel inanimate object (lighter colors) for WT (grey) and Shank3$^{-/-}$ (blue).

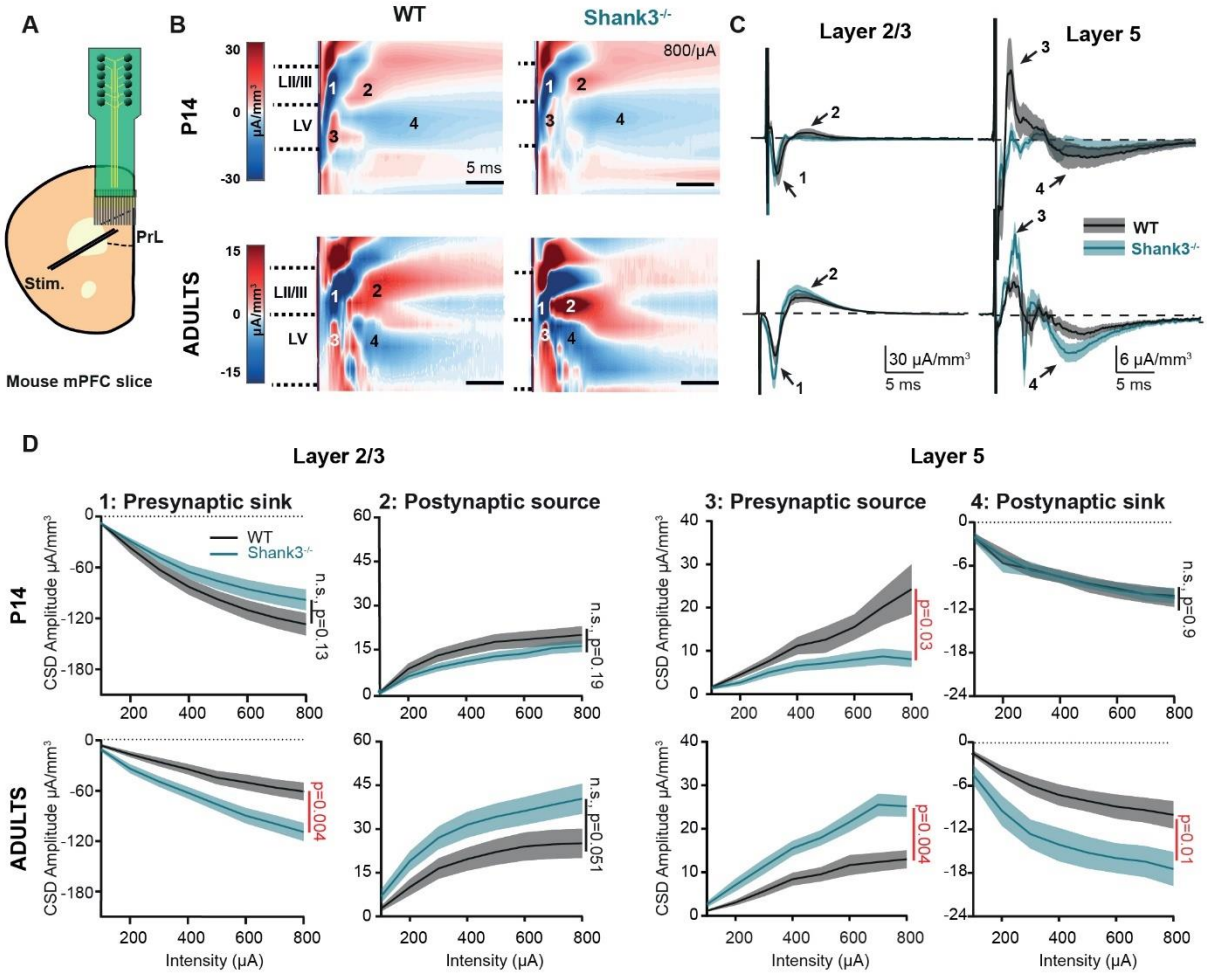

Figure 2. Shank3$^{-/-}$ mice display mPFC hypofunction in early life and hyperfunction in adulthood. (A) Schematic of LFP recording across all mPFC layers in response to electrical stimulation delivered to deep layers. (B) Average current source density (CSD) response displayed as a heat map of mPFC network activity in response to a near maximal (800μA) stimulation in WT (left) and Shank3$^{-/-}$ (right) at P14 (top row; WT= 3 mice, 10 slices; Shank3$^{-/-}$ = 3 mice, 11 slices) and adults (>P55, bottom row; WT= 5 mice, 12 slices; Shank3$^{-/-}$= 5 mice, 13 slices). (C) Average CSD response of the L2/3 presynaptic sink (arrow 1, numbers correspond to those in B), L2/3 postsynaptic source (arrow 2), L5 presynaptic source (arrow 3) and L5 postsynaptic sink (arrow 4) in P14 (upper) and adult (lower) slices. Traces represent mean (solid line) ± sem (shaded line). (D) Input/ Output curve of CSD peak amplitude as a function stimuli intensity for P14 (top row) and adults (bottom row); WT (grey) and Shank3$^{-/-}$ (blue).

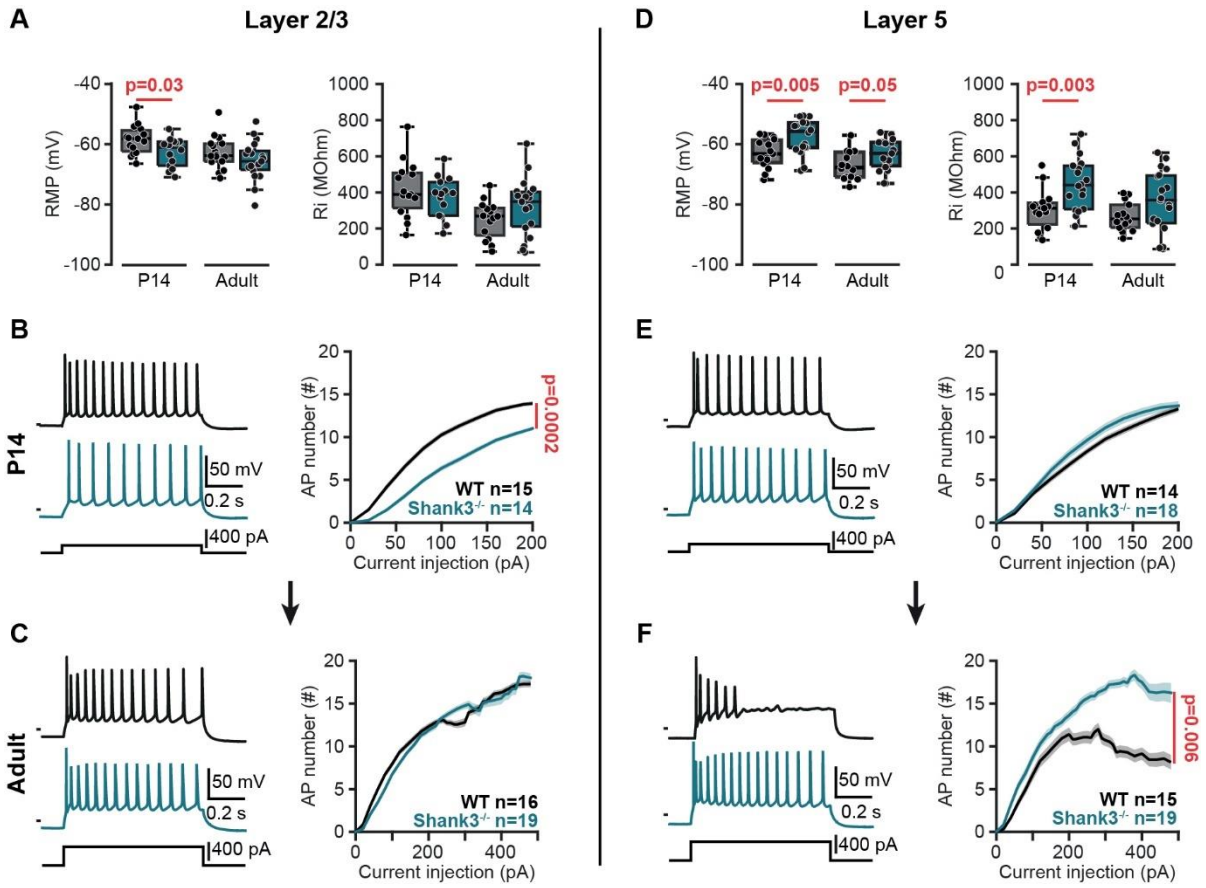

Figure 3. Shank3$^{-/-}$ mice display early electrophysiological hypoexcitability in mPFC layer 2/3 that develops into hyperexcitability of layer 5 in adulthood. (A) Resting membrane potential (RMP, left) and input resistance (Rm, right) of layer 2/3 pyramidal neurons from P14 and adult WT (grey) and Shank3$^{-/-}$ (blue) mice. (B) Left, representative action potential trains in layer 2/3 mPFC pyramidal cells in response to 100 pA, 1s current injection at P14. Right, number of APs in layer 2/3 pyramidal cells at P14. Traces represent mean ± sem. (C) Same as (B) in adult mice. (D) Resting membrane potential (RMP, left) and input resistance (Rm, right) of layer 5 pyramidal neurons from P14 and adult WT (grey) and Shank3$^{-/-}$ (blue) mice. (E) Left, representative action potential responses of layer 5 mPFC pyramidal cells at P14 (400 pA stimulus). Right, number of APs in layer 5 pyramidal cells at P14. Traces represent mean ± SEM. (F) Same as (E) in adult mice.

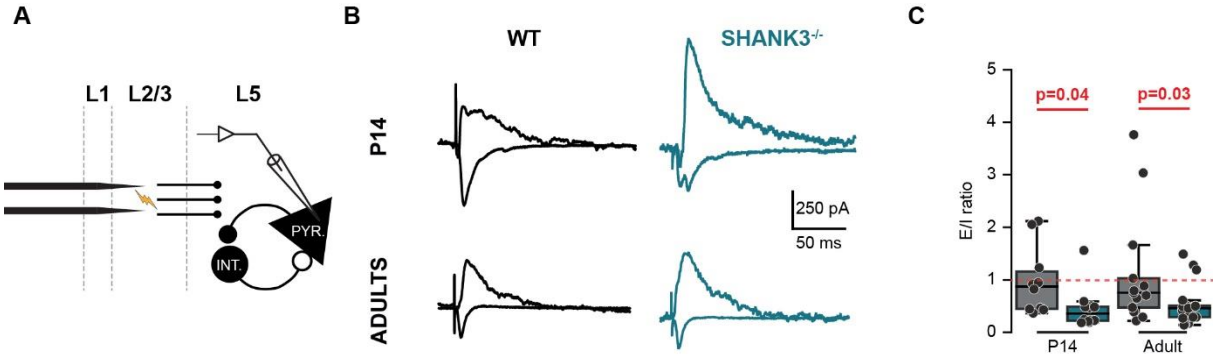

Figure 4. Excitatory/inhibitory synaptic current ratio is reduced in Shank3$^{-/-}$ mPFC L5 pyramidal cells at both P14 and in adults. (A) Experimental design to measure EPSCs (at -70 mV) and IPSCs (at +10 mV) in mPFC slices, with electrical stimulation of layer 2/3. (B) Representative Excitatory and Inhibitory synaptic current responses elicited in mPFC layer 5 pyramidal cells by an electrical stimulation in layer 2/3 of P14 (top) and adult (bottom) WT (grey) and Shank3$^{-/-}$ (blue) mice. (C) E/I ratio at P14 (left panel; WT (grey), 4 mice, 10 cells; Shank3$^{-/-}$ (blue), 5 mice, 12 cells) and adulthood (right panel; WT (grey), 7 mice, 11 cells; Shank3$^{-/-}$ (blue), 7 mice, 15 cells).

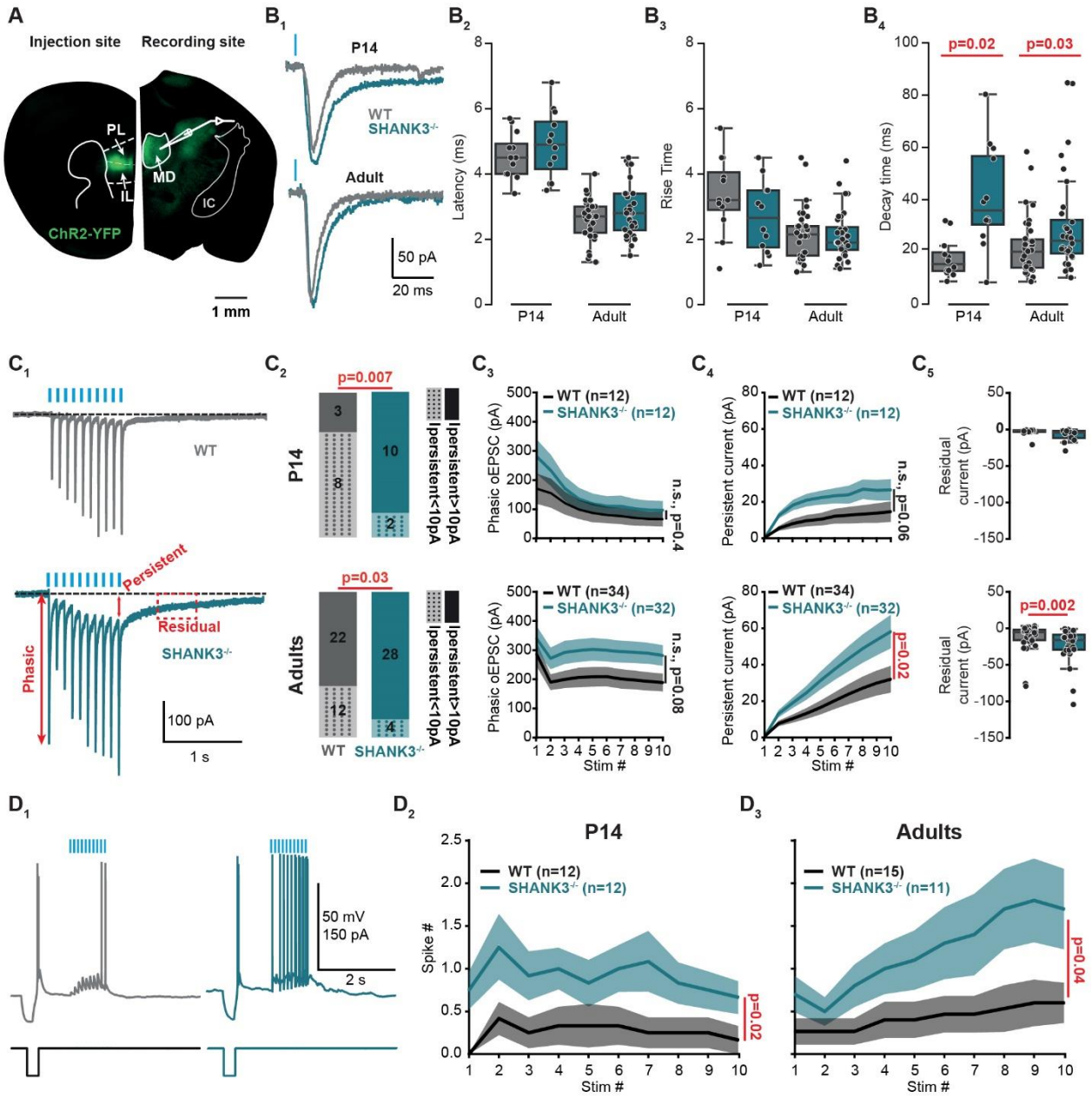

Figure 5. Enhanced mPFC-MD synaptic function in P14 and adult Shank3$^{-/-}$ mice. (A) Epifluorescence image showing the injection site of AAV1_ChR2_YFP in mPFC (left) and labeled projections in MD thalamus (right). (B1) Representative optogenetically-evoked EPSC (oEPSC, phasic responses) from MD neurons of WT (grey) and Shank3$^{-/-}$ (blue) mice. Data from P14 animals are shown on the top, while adult data are shown on the bottom. (B2-B4) Phasic oEPSC latency, rise time, and decay time for P14 (left) WT (grey, 2 mice, 12 cells) and Shank3$^{-/-}$ (blue, 2 mice, 11 cells), and for adults (right) WT (grey, 16 mice, 34 cells) and Shank3$^{-/-}$ (blue, 12 mice, 32 cells). (C1) Representative oEPSC trains elicited by 10 Hz stimulation. Phasic, persistent, and residual current measurements are indicated in red. (C2-5) P14 (top), Adult (bottom). (C2)

805 Proportions of cells with detectable (>10 pA) or undetectable (<10 pA) persistent current ($I_{persistent}$) in MD
806 cells of WT (grey) and Shank3$^{-/-}$ (blue) mice. (C3) Averaged phasic current amplitude with 10 Hz stimulation
807 for WT (grey) and Shank3$^{-/-}$ (blue) mice. (C4) Averaged persistent current with 10 Hz stimulation for WT
808 (grey) and Shank3$^{-/-}$ (blue) mice. (C5) Residual responses in WT (grey) and Shank3$^{-/-}$ (blue) mice. (D1)
809 Representative traces of current-clamp recordings from MD cells upon repeated activation of mPFC axons.
810 (D2) Number of evoked action potentials during oEPSC trains from P14 WT (black) and Shank3$^{-/-}$ (blue)
811 mice. (D3) Evoked action potentials from adult WT (black) and Shank3$^{-/-}$ (blue) mice. Traces represent
812 mean ± SEM.

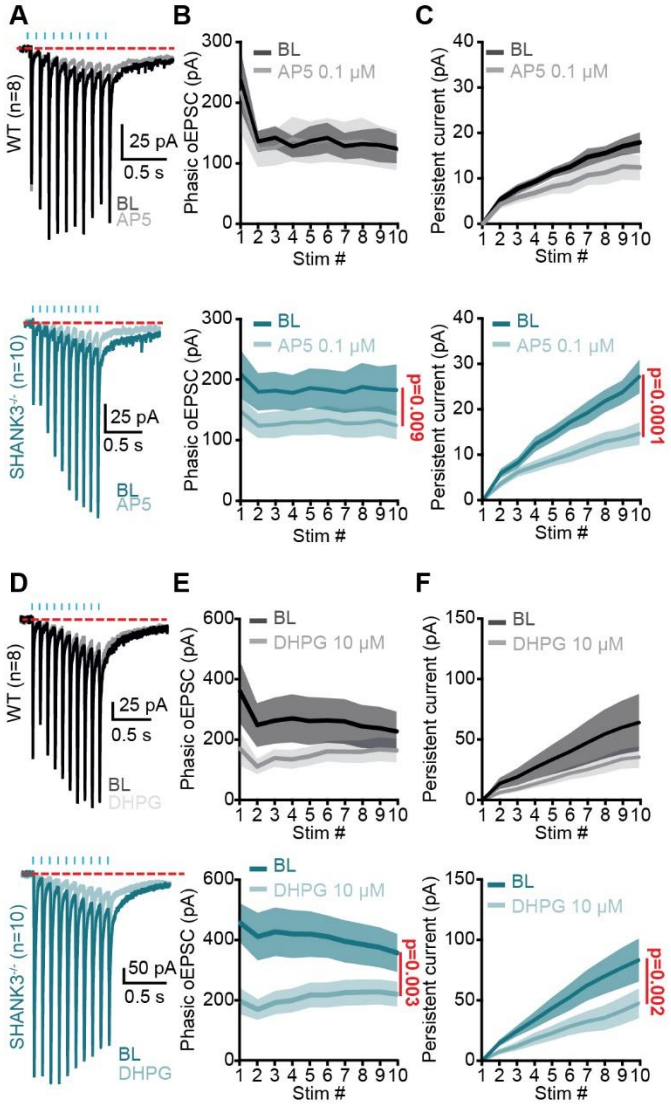

Figure 6. mGluR and NMDAR contribution to the phasic and persistent mPFC response to oEPSCs especially in Shank3$^{-/-}$ mice. (A) Representative oEPSCs elicited with 10Hz stimulation in MD before (dark color) and after 0.1uM AP5 (light color) for WT (grey, 6 mice, 8 cells) and Shank3$^{-/-}$ (blue, 3 mice, 10 cells) mice. (B) Peak amplitude of phasic currents in response to 10Hz stimulation in WT (top, grey) and Shank3$^{-/-}$ (bottom, blue) mice before (BL, baseline, dark color) and during AP5 bath application (AP5 0.1uM, light color). (C) Same as (B) for persistent current. (D) Representative oEPSCs elicited with 10Hz stimulation in MD before (dark color) and after 10uM DHPG (light color) for MD recordings from WT (grey, 3 mice, 8 cells) and Shank3$^{-/-}$ (blue, 4 mice, 12 cells) mice. (E) MD phasic current with 10Hz stimulation for WT (top, grey) and Shank3$^{-/-}$ (bottom, blue) mice before (BL, baseline, dark color) and during AP5 bath application (AP5 0.1uM, light color). (F) Same as (E) for persistent current. Traces are represented are mean (solid line) ± sem (shaded line).